

Augmented Lagrangian Solvers for Poroelasticity with Fracture Contact Mechanics

Marius Nevland^{1*}, Inga Berre¹, Jakub Wiktor Both¹, Eirik Keilegavlen¹

¹Center for Modeling of Coupled Subsurface Dynamics, Department of Mathematics, University of Bergen, Allégaten 41, Bergen, 5020, Norway.

*Corresponding author(s). E-mail(s): marius.nevland@uib.no;

Contributing authors: inga.berre@uib.no; jakub.both@uib.no; eirik.keilegavlen@uib.no;

Abstract

In the subsurface, fractures and the surrounding porous rock can deform in interaction with fluid flow. Advanced mathematical models governing these coupled processes typically combine fluid flow, poroelasticity, and fracture contact mechanics, representing fractures as co-dimension one objects within the porous medium. The resulting system of equations is complex and highly nonlinear. As a result, convergence issues with nonlinear solvers are common, which hinders the practical implementation of such models.

One particular source of difficulty for the nonlinear solvers comes from the fracture contact mechanics, due to its inherently nonsmooth character. In this paper, we investigate solvers based on the augmented Lagrangian formulation of the frictional contact problem. This includes two classical solvers, namely the generalized Newton method (using complementarity functions) and the return map method. In addition, we propose a new augmented Lagrangian solver that combines the two approaches.

Numerical experiments in two and three dimensions are conducted to assess the performance of the solvers on problems of mixed-dimensional poromechanics with fracture contact mechanics. The experiments indicate that for simpler setups, the solvers behave quite predictably and in accordance with established heuristics from the contact mechanics literature. However, as the complexity of the problem increases, the solvers become more unpredictable, and break with these heuristics. In particular, the two classical solvers become highly sensitive to the augmentation parameter. The new solver converges across a larger range of this parameter in most cases, but nevertheless also displays unpredictable behavior.

Keywords: Fractured porous media, poroelasticity, contact mechanics, augmented Lagrangian, generalized Newton, return map

1 Introduction

The mathematical modeling and simulation of coupled flow and deformation in fractured porous media has numerous important applications, such as in CO₂ storage and geothermal energy production. The

tightly coupled physical processes, combined with the discontinuous nature of fractures and the structural complexity of fracture networks, result in significant mathematical challenges, from a modeling as well as a numerical perspective.

An overview of different conceptual approaches to model fractured porous media can be found in [1–3]. In this work, we specifically consider discrete fracture-matrix models, in which the fractures are explicitly represented. Specifically, the matrix (i.e. the porous medium surrounding the fractures) is modeled as linearly poroelastic [4] with flow governed by Darcy’s law. For the fracture, Darcy flow is also considered, while deformation is modeled by contact mechanics including Coulomb friction [5]. There have been several recent works on such models [6–14], focusing on the development of discretization methods adapted to the discrete fracture-matrix model. In this context, for the mechanical subproblem, a common approach is to use finite element methods [10–14], but, motivated by the coupling with flow, finite volume methods are also increasingly being applied [6–9]. The flow equations are usually discretized by finite volume methods [6–13], but finite element methods have also been used [14]. In addition, considerable efforts have been made to stabilize the mechanical subproblem [12, 15, 16].

To apply these discretization schemes to complex setups that reflect the physical states and fractured structures encountered in field applications, there is a need for nonlinear solvers for discrete fracture-matrix models for poromechanics, and scalable linear solvers. Linear solvers, based on block preconditioning that is tailored to both the individual physical processes and their couplings, have been developed for both finite element [17–19] and finite volume [20, 21] discretizations. In terms of nonlinear solvers, a challenging aspect is the inherent nonlinear and nonsmooth character of frictional contact problems [5, 22]. Several classes of nonlinear solvers that were originally developed for frictional contact mechanics have been extended to account for poromechanics. These solvers are built around different ways of formulating the contact conditions, and includes solvers based on the penalty [10], augmented Lagrangian [6, 23] and Nitsche formulations [11, 12] of the frictional contact problem. However, the poromechanical coupling introduces new challenges for the nonlinear solvers: First, the extra couplings make for larger and more complex algebraic systems. Second, depending on model choices, the systems might contain other nonlinearities that are triggered by the contact mechanics, such as shear dilation of fractures and fracture permeability modeled by a cubic law [7, 8]. As a result, the design of robust nonlinear solvers for these problems remains a challenge that must be addressed to enable reliable simulations with advanced physical models on complex fracture geometries.

The focus of this paper is on nonlinear solvers based on the augmented Lagrangian formulation of frictional contact mechanics. It may be viewed as a combination of the Lagrange multiplier and penalty formulations, inheriting favorable properties from both. An important feature of the augmented Lagrangian formulation, as well as the penalty formulation, is the presence of a numerical parameter which must be chosen by the user (we will henceforth refer to it as the *augmentation parameter*). This parameter can be interpreted as regularizing the problem, although the solution to the augmented Lagrangian formulation will still be exact for any positive value of the parameter. This is in contrast to the penalty formulation, where the original solution is only recovered as the augmentation parameter goes to infinity. While the augmented Lagrangian formulation is a popular choice for solving problems involving contact mechanics, it is still prone to convergence issues. This is demonstrated in [24], where several nonlinear solvers, among which solvers based on the augmented Lagrangian formulation, were tested on a range of purely mechanical contact problems for non-fractured media. The solvers failed to converge in several cases, with the performance often being very sensitive to the value of the augmentation parameter. The present work can be viewed as an extension of the parts of the study in [24] concerning the augmented Lagrangian solvers, to assess the performance of these solvers on problems of coupled flow and deformation including fracture contact mechanics.

There are two distinct classical nonlinear solvers based on the augmented Lagrangian formulation of frictional contact mechanics. The first approach is based on a reformulation of the variational inequalities of contact mechanics as the zero sets of certain non-smooth functions called complementarity functions. This enables the use of a generalized Newton method with appropriately defined generalized Jacobians to handle the system’s non-smoothness. This approach was first introduced by Alart and Curnier [25], and several different ways of formulating the complementarity functions have since been derived [26, 27]. The second approach, introduced by Simo and Laursen [28], uses a fixed-point iteration on the augmented Lagrange multipliers, resulting in a return map method that can also be interpreted as an Uzawa algorithm [24]. We note that the algorithm in [28] corresponds to an *implicit* version of the Uzawa

algorithm, which is known to improve the stability of the algorithm [29], at the cost of needing to solve a more complicated system.

Both the generalized Newton method and the return map method will be considered in this work. Moreover, we will provide a formal connection between these two methods. More specifically, we will demonstrate that the return map method is equivalent to solving a sequence of nonlinear systems with regularized complementarity functions, where each of these systems can be solved by the generalized Newton method. This observation leads us to propose a new nonlinear solver, in which we incorporate the return map into the generalized Newton method as a postprocessing step. This approach allows the return map to be applied without requiring regularization of the equations.

To illustrate the convergence challenges and evaluate the performance of the generalized Newton method, the return map method, and our new nonlinear solver, we carry out a series of numerical experiments in both two and three dimensions. These experiments are inspired by hydraulic stimulation of geothermal reservoirs, in which critically stressed fractures are stimulated by fluid injection, resulting in fracture slip and opening. Simulations are conducted across a range of injection pressures, as well as a range of shear dilation angles, highlighting how the coupling between flow and mechanics evolves and contributes to convergence difficulties for the nonlinear solvers. We also investigate a range of values for the augmentation parameter to assess whether established heuristics from contact mechanics can inform its selection in this context.

The remainder of the paper is structured as follows. In Section 2, we present the mathematical model for coupled flow and deformation in fractured porous media. Section 3 introduces the generalized Newton method and the return map method, adapted to the governing equations, and establishes a formal connection between them. This connection motivates the development of our new nonlinear solver, which is subsequently introduced. In Section 4, we evaluate the performance of all three nonlinear solvers through a series of numerical experiments. Concluding remarks are provided in Section 5.

2 Mathematical model

We consider a discrete fracture-matrix model, where the fractures are modeled as co-dimension one objects, leading to a mixed-dimensional poromechanical model including fracture contact mechanics. The presentation of the model in this section closely follows that of [8]; see also [6, 7, 30]. We first give an overview of the mixed-dimensional geometry in section 2.1. In section 2.2, conservation laws for mass and momentum balance, with corresponding constitutive laws, are presented. The equations of fracture contact mechanics are presented in section 2.3. Finally, in section 2.4 we define the boundary conditions and provide a summary of the primary variables and equations.

2.1 Mixed-dimensional geometry

The fractured porous medium is described as a collection of subdomains Ω_i of varying dimension $d_i \in \{0, \dots, D\}$, with $D \in \{2, 3\}$. The matrix subdomain will have dimension D , while fractures are modeled as co-dimension one objects, and will accordingly have dimension $D - 1$. Moreover, intersections of fractures will have dimension $D - 2$, and in the case of $D = 3$, one also considers intersections of fracture intersection lines as zero-dimensional subdomains. The width of a fracture is characterized by its aperture a_i . This is further generalized by introducing the specific volume $\mathcal{V}_i = a_i^{D-d_i}$, accounting for dimension reduction for a subdomain Ω_i with any dimension $d_i \leq D$.

A pair of subdomains one dimension apart will always be connected by one or more interfaces Γ_j, Γ_k . This is done to facilitate the coupling of processes between subdomains of varying dimension. For such a pair of subdomains, it will be convenient to denote the higher-dimensional subdomain by Ω_h and the lower-dimensional one by Ω_l . As illustrated in figure 1, the interfaces Γ_j, Γ_k will geometrically coincide with Ω_l and the internal boundaries $\partial_j \Omega_h, \partial_k \Omega_h$ of Ω_h . It is sometimes necessary to project relevant quantities from a subdomain to an interface or vice versa. The projection from a subdomain Ω_i to an interface Γ_j is denoted by Π_j^i , while the reverse operation is denoted by Ξ_j^i .

Subscripts will be used to denote on which subdomain or interface a quantity is defined. A generic subdomain and interface are denoted by subscripts i and j , respectively. If two interfaces are involved, we will use subscript k for the second interface. For certain equations involving couplings between a higher- and lower-dimensional subdomain, we use subscript h for the higher dimension and l for the lower dimension.

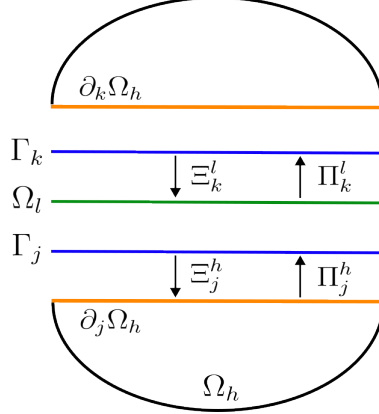


Fig. 1 Illustration of the mixed-dimensional geometry. The higher-dimensional subdomain Ω_h is coupled to the lower-dimensional subdomain Ω_l through the interfaces Γ_j and Γ_k . Note that $\partial_j\Omega_h$, $\partial_k\Omega_h$, Γ_j , Γ_k and Ω_l all coincide geometrically. Figure adapted from [7]

2.2 Conservation laws and constitutive relations

Mixed-dimensional conservation laws establish the foundation for the communication across the different dimensions. The fluid mass conservation equation for a general subdomain Ω_i of dimension $d_i \in \{0, \dots, D\}$ reads:

$$\frac{\partial}{\partial t}(\mathcal{V}_i \rho_i^f \phi_i) + \nabla \cdot (\mathcal{V}_i \rho_i^f \mathbf{v}_i) - \sum_{j \in \hat{S}_i} \Xi_j^i (\mathcal{V}_j \rho_j^f v_j) = \psi_i, \quad (1)$$

where ρ_i^f, ρ_j^f are the subdomain and interface fluid densities, respectively, ϕ_i is the porosity, \mathbf{v}_i and v_j are the subdomain and interface volumetric fluid fluxes, ψ_i is a source term, $\mathcal{V}_j := \Pi_j^i \mathcal{V}_i$ is the interface specific volume, and the set \hat{S}_i contains all interfaces connecting to higher-dimensional neighbors of Ω_i . The second term on the left hand side of (1) vanishes for $d_i = 0$, as zero-dimensional domains do not have mass fluxes, while the third term on the left hand side of (1) vanishes for $d_i = D$, in which case there are no higher-dimensional neighboring subdomains.

Assuming a quasi-static process, the momentum balance equation of the matrix subdomain ($d_i = D$) reads:

$$-\nabla \cdot \boldsymbol{\sigma} = \mathbf{F}, \quad (2)$$

with $\boldsymbol{\sigma}$ being the total poroelastic stress tensor and \mathbf{F} denoting body forces.

Next, we define constitutive relations for the various quantities defined above, most of which are derived from [4]. The volumetric fluid flux is modeled by Darcy's law:

$$\mathbf{v}_i = -\frac{\mathcal{K}_i}{\eta} (\nabla p_i - \rho_i^f \mathbf{g}), \quad (3)$$

where η is the viscosity (assumed to be constant), p_i is the pressure, \mathcal{K}_i is the permeability tensor and \mathbf{g} the gravitational acceleration vector. In order to define the constitutive laws for the permeabilities, we first define \mathbf{I}_D and \mathbf{I}_{D-1} to be the identity matrices of dimension D and $D-1$, respectively. The permeability tensor \mathcal{K}_i is assumed to be spatially homogeneous in the matrix, hence it is a constant multiple k of the identity matrix:

$$\mathcal{K}_i = k \mathbf{I}_D \quad , \quad d_i = D, \quad (4)$$

while in fracture subdomains, it is given by a cubic law [31]:

$$\mathcal{K}_i = \frac{a_i^2}{12} \mathbf{I}_{D-1} \quad , \quad d_i = D - 1. \quad (5)$$

Finally, intersection permeability is computed as the average permeability of the intersecting fractures. Solid density is assumed to be constant, while the density of the slightly compressible fluid is given by (we omit the subscript i for readability):

$$\rho^f = \rho_{\text{ref}}^f \exp(\gamma(p - p_{\text{ref}})), \quad (6)$$

where γ is the compressibility of the fluid. The subscript "ref" is used to denote reference values of variables. The interface flux v_j is given by an averaged Darcy's law [32]:

$$v_j = -\frac{\mathcal{K}_j}{\eta} \left(\frac{2}{\Pi_j^l a_l} (\Pi_j^l p_l - \Pi_j^h p_h) - \rho_j^f \mathbf{g} \cdot \Pi_j^h \mathbf{n}_h \right). \quad (7)$$

Here, \mathbf{n}_h is the outward normal vector of the higher-dimensional neighboring subdomain. The interface permeability \mathcal{K}_j is also modeled by a cubic law, inheriting the aperture from its lower-dimensional neighboring subdomain,

$$\mathcal{K}_j = \frac{\Pi_j^l a_l^2}{12}, \quad (8)$$

while the interface fluid density ρ_j^f is defined by an upstream weighting based on the direction of v_j :

$$\rho_j^f = \begin{cases} \Pi_j^h \rho_h^f & \text{if } v_j > 0, \\ \Pi_j^l \rho_l^f & \text{if } v_j \leq 0. \end{cases} \quad (9)$$

The total poroelastic stress tensor is given by an extended Hooke's law that also accounts for fluid pressure:

$$\boldsymbol{\sigma} = G(\nabla \mathbf{u} + \nabla \mathbf{u}^T) + \lambda_{\text{Lamé}} \text{tr}(\nabla \mathbf{u}) \mathbf{I}_D - \alpha p \mathbf{I}_D. \quad (10)$$

Here, \mathbf{u} denotes the displacement, G is the shear modulus, $\lambda_{\text{Lamé}}$ is Lamé's first parameter, α is the Biot coefficient and $\text{tr}(\cdot)$ denotes the trace of a matrix. The porosity of fractures and intersections is set to one, while the matrix porosity depends on displacement and pressure as follows:

$$\phi = \phi_{\text{ref}} + \frac{(\alpha - \phi_{\text{ref}})(1 - \alpha)}{\lambda_{\text{Lamé}} + \frac{2}{3}G} (p - p_{\text{ref}}) + \alpha(\nabla \cdot \mathbf{u}). \quad (11)$$

The body force in the momentum balance equation (2) is given as the combined gravitational forces of the solid and the fluid:

$$\mathbf{F} = (\phi \rho^f + (1 - \phi) \rho^s) \mathbf{g}, \quad (12)$$

where ρ^s is the solid density. The only constitutive law now remaining is the one for the aperture a_i ; this will be defined in section 2.3, after some new notation has been introduced.

2.3 Fracture contact mechanics

The equations of contact mechanics are imposed on pairs of D -dimensional matrix subdomains Ω_h and $D-1$ -dimensional fracture subdomains Ω_l that are connected through two interfaces Γ_j, Γ_k , as illustrated in figure 1. Some new variables are introduced: The fracture contact traction $\boldsymbol{\lambda}_l$, defined on the fracture domain Ω_l , and the displacements $\mathbf{u}_j, \mathbf{u}_k$ of the interfaces Γ_j, Γ_k . For readability purposes, we will omit the subscript l from the contact traction. The forces on the two fracture surfaces must be balanced according to Newton's third law. Taking into account that the pressure from the fluid in the fracture contributes to the total fracture traction, the following balance of forces are imposed at the interfaces:

$$\begin{aligned} \Pi_j^l (\boldsymbol{\lambda} - p_l \mathbf{I}_D \cdot \mathbf{n}_l) &= \Pi_j^h \sigma_h \cdot \mathbf{n}_h & \text{on } \Gamma_j, \\ \Pi_k^l (\boldsymbol{\lambda} - p_l \mathbf{I}_D \cdot \mathbf{n}_l) &= -\Pi_k^h \sigma_h \cdot \mathbf{n}_h & \text{on } \Gamma_k, \end{aligned} \quad (13)$$

where \mathbf{n}_l denotes the normal vector of the fracture, which is defined as $\mathbf{n}_l = \Xi_j^l \Pi_j^h \mathbf{n}_h$. In other words, it is chosen to equal \mathbf{n}_h on the j side. A vector \mathbf{v} defined on a fracture may be decomposed into its normal and tangential components with respect to the fracture as follows:

$$v_n = \mathbf{v} \cdot \mathbf{n}_l, \quad \mathbf{v}_\tau = \mathbf{v} - v_n \mathbf{n}_l. \quad (14)$$

The jump in interface displacements across Ω_l is defined as $[[\mathbf{u}]] = \Xi_k^l \mathbf{u}_k - \Xi_j^l \mathbf{u}_j$. The relative movement of the fracture is restricted by a nonpenetration condition, which can be written as:

$$\begin{aligned} [[\mathbf{u}]]_n - g &\geq 0, \\ \lambda_n &\leq 0, \\ \lambda_n ([[\mathbf{u}]]_n - g) &= 0, \end{aligned} \quad (15)$$

where g is the gap function, which should have the property that $[[\mathbf{u}]]_n - g = 0$ when the surfaces are in contact, and $[[\mathbf{u}]]_n - g > 0$, otherwise. The constitutive law for g depends on modeling choices. In this work we use a formula that incorporates shear dilation of fractures. Due to small scale surface roughness of a fracture, displacement along the fracture can cause shear dilation, resulting in the fracture being mechanically closed but hydraulically open. This effect is incorporated into the model by defining a dilation angle ψ , and choosing the gap function to be

$$g(\mathbf{u}) = \tan(\psi) \| [[\mathbf{u}]]_\tau \|. \quad (16)$$

This definition results in g having the aforementioned properties. Next, we require the tangential surface traction to satisfy the Coulomb friction law in the case of contact, while it should vanish in the case of no contact:

$$\begin{cases} \text{If } \lambda_n = 0 \implies \boldsymbol{\lambda}_\tau = \mathbf{0}. \\ \text{Else :} \\ \quad \|\boldsymbol{\lambda}_\tau\| \leq -F \lambda_n, \\ \quad \|\boldsymbol{\lambda}_\tau\| < -F \lambda_n \implies [[\dot{\mathbf{u}}]]_\tau = \mathbf{0}, \\ \quad \|\boldsymbol{\lambda}_\tau\| = -F \lambda_n \implies \exists \zeta \in \mathbb{R}^+ : [[\dot{\mathbf{u}}]]_\tau = \zeta \boldsymbol{\lambda}_\tau, \end{cases} \quad (17)$$

where F is the coefficient of friction and $[[\dot{\mathbf{u}}]]_\tau$ is the time derivative of the tangential displacement jump. We will for convenience refer to the entirety of equation (17) as the Coulomb friction law. Finally, we define the constitutive law for the aperture. In fracture subdomains, we set the aperture to equal the normal component of the interface displacement jump, with an additional constant reference aperture a_{ref} taking into account small-scale roughnesses in the undeformed state:

$$a = a_{\text{ref}} + [[\mathbf{u}]]_n. \quad (18)$$

For intersection subdomains ($d_i < D - 1$), the aperture is computed as the average aperture of the intersecting fractures:

$$a_i = \frac{1}{|\hat{S}_i|} \sum_{j \in \hat{S}_i} \Xi_j^i \Pi_j^h a_h. \quad (19)$$

2.4 Boundary conditions and summary

Boundary conditions are imposed on both internal and external boundaries. On the internal boundaries $\partial_j \Omega_i$, we require continuity of normal mass fluxes and displacements (the latter only applies for $d_i = D$):

$$\mathcal{V}_i \rho_i^f \mathbf{v}_i \cdot \mathbf{n}_i = \Xi_j^i \mathcal{V}_j \rho_j^f v_j, \quad (20)$$

$$\mathbf{u}_i = \Xi_j^i \mathbf{u}_j. \quad (21)$$

On external boundaries, we impose either Dirichlet or Neumann boundary conditions. The mechanical boundary data is accordingly either prescribed values of displacement \mathbf{u} or traction $\boldsymbol{\sigma} \cdot \mathbf{n}$, and fluid boundary data is either prescribed values of pressure p or mass flux $\rho \mathbf{v} \cdot \mathbf{n}$. Finally, we impose zero fluid mass flux on immersed fracture tips, supported by the discussion in [33].

A summary of the system of equations and primary variables to be solved for is outlined in table 1.

Equations	Variables	Subdomains or interfaces
Mass balance, (1)	Pressure p_i	Ω_i for all d_i
Momentum balance, (2)	Displacement \mathbf{u}_i	Ω_i for $d_i = D$
Interface Darcy flux, (7)	Interface Darcy flux v_j	Γ_j for all d_j
Interface force balance, (13)	Interface displacement \mathbf{u}_j	Γ_j for $d_j = D - 1$
Nonpenetration condition, (15)	Contact traction $\boldsymbol{\lambda}$	Ω_i for $d_i = D - 1$
Coulomb friction law (17)		Ω_i for $d_i = D - 1$

Table 1 Summary of equations and primary variables, as well as the subdomains or interfaces on which they are defined. The equation and variable on a specific row are both defined on the same subdomains or interfaces, which is specified in the same row.

3 Augmented Lagrangian solvers

In this section, we will present three different nonlinear solvers for the system of equations presented in the previous section. All three solvers are based on the augmented Lagrangian formulation of the frictional contact problem. Two of these solvers are classical, namely the generalized Newton method and the implicit return map, while the third solver is new. To ease the presentation and stress their agnostic character to spatial discretizations, the solvers will be presented in a semi-discrete setting, where the equations are assumed to be discretized in time, using the implicit Euler method, but continuous in space. As a consequence, the slip velocity $[[\dot{\mathbf{u}}]]_\tau$ now refers to the time increment of the tangential displacement jump, i.e. $[[\dot{\mathbf{u}}]]_\tau = [[\mathbf{u}]]_\tau - [[\mathbf{u}]]_\tau^{\text{prev}}$, where "prev" denotes the previous time step, and the time step size is implicitly subsumed in the scaling constant in (17). We will give some details in section 3.4 of the particular spatial discretizations used in the numerical experiments of the present work.

Notation. We denote nonlinear iteration indices by superscripts. Moreover, it will be convenient to separate the contact conditions (15), (17) from the rest of the equation system, as the contact conditions are treated differently, depending on the solver, while the residual system remains unchanged. We denote the residual system by G , and collect all unknowns into a vector \mathbf{x} . Hence, the equation

$$G(\mathbf{x}) = \mathbf{0}, \quad (22)$$

describes the semi-discrete formulations of all equations from table 1, with the exception of (15) and (17), at a particular time step.

3.1 The generalized Newton method

The nonpenetration condition (15) and Coulomb friction law (17) can be reformulated as the zero sets of certain nonsmooth functions called complementarity functions. Such a reformulation can be derived from a theoretical consideration of the augmented Lagrangian formulation of the contact problem, as shown in [25]. There are several ways of formulating these complementarity functions [25–27]. In the present work, we employ the formulation of Hübner et al. [27], in which it is shown that, for every augmentation parameter $c > 0$, the nonpenetration condition (15) is equivalent to:

$$\mathcal{C}_n := \lambda_n + \max(0, -\lambda_n - c([[\mathbf{u}]]_n - g(\mathbf{u}))) = 0. \quad (23)$$

Similarly, for every $c > 0$, the Coulomb friction law (17) is equivalent to:

$$\mathcal{C}_\tau := \chi \boldsymbol{\lambda}_\tau + (1 - \chi) [b(\boldsymbol{\lambda}_\tau + c[[\dot{\mathbf{u}}]]_\tau) - \max(b, \|\boldsymbol{\lambda}_\tau + c[[\dot{\mathbf{u}}]]_\tau\|) \boldsymbol{\lambda}_\tau] = \mathbf{0}. \quad (24)$$

Here $b = -F\lambda_n$ is the friction bound and χ is a characteristic function that equals 1 if $b \leq 0$ and 0 if $b > 0$, thus enforcing $\boldsymbol{\lambda}_\tau = \mathbf{0}$ in the case of no contact. By replacing (15) and (17) with (23) and (24), the entire equation system of table 1 may be written compactly in residual form. Using the previously

defined residual system (22), the full system of equations to be solved at a specific time step reads

$$F(\mathbf{x}) := \begin{bmatrix} G(\mathbf{x}) \\ \mathcal{C}_n(\mathbf{x}) \\ \mathcal{C}_\tau(\mathbf{x}) \end{bmatrix} = \mathbf{0}. \quad (25)$$

This system is only differentiable almost everywhere (in the sense of the Lebesgue measure), due to the non-smoothness of the complementarity functions. However, the non-differentiable points can easily be handled by employing generalized derivatives, using the definition found in Clarke [34]. A set of generalized Jacobians for the system (25) at a point \mathbf{x}^* is defined as follows:

$$\partial F(\mathbf{x}^*) = \text{conv} \left\{ \lim_{\mathbf{x}_i \rightarrow \mathbf{x}^*, \mathbf{x}_i \in \Omega_F} DF(\mathbf{x}_i) \right\}, \quad (26)$$

where Ω_F is the set of points on which F is differentiable, with corresponding Jacobian DF , and "conv" denotes the convex hull. Using these generalized Jacobians, a corresponding generalized Newton method can be defined [25, 27], which is described below. We will abbreviate the method by GNM.

Algorithm 1 Generalized Newton Method (GNM)

1. Pick an initial guess $\mathbf{x}^{(0)}$. Set $k = 0$.
2. Solve for $\mathbf{x}^{(k+1)}$ the Newton linearization of system (25) at $\mathbf{x}^{(k)}$:

$$V^{(k)}(\mathbf{x}^{(k+1)} - \mathbf{x}^{(k)}) = -F(\mathbf{x}^{(k)}), \quad (27)$$

where $V^{(k)} \in \partial F(\mathbf{x}^{(k)})$.

3. Convergence check:
 - if** $\mathbf{x}^{(k+1)}$ fulfills convergence criterion **then**
 - Exit algorithm.
 - else**
 - Set $k = k + 1$ and go to 2.
-

Let us briefly comment on the augmentation parameter c appearing in the complementarity functions. Since the two complementarity functions are an exact reformulation of the nonpenetration condition (15) and Coulomb friction law (17) for all $c > 0$, this parameter may be chosen freely without affecting the accuracy of the solution. This reflects the fact that the solution to the augmented Lagrangian formulation is exact for all positive values of the augmentation parameter, as mentioned in the introduction. It is important to note, however, that the choice of the parameter can greatly affect the performance of the generalized Newton method (this is also the case for the other nonlinear solvers considered in this work); this will be shown in the numerical experiments of section 4.

Following [7, 27], we define "generalized" contact states, based on the arguments of the maximum functions of (23) and (24). We group open, stick and slip states as follows:

$$\begin{aligned} \text{Open} &= \{-\lambda_n - c([\mathbf{u}]_n - g) \leq 0\}, \\ \text{Stick} &= \{b > 0 \text{ and } \|\boldsymbol{\lambda}_\tau + c[[\dot{\mathbf{u}}]]_\tau\| < b\}, \\ \text{Slip} &= \{b > 0 \text{ and } \|\boldsymbol{\lambda}_\tau + c[[\dot{\mathbf{u}}]]_\tau\| \geq b\}. \end{aligned} \quad (28)$$

The physical contact states of open, stick and slip, as described by the nonpenetration condition (15) and Coulomb friction law (17), are subsets of the corresponding sets above, hence the notion of generalized contact states. References to the sets (28) will be made in section 4.

3.2 The implicit return map method

Return map methods are commonly used in computational plasticity [35, 36], and have also been applied to frictional contact problems [28, 37, 38]. The defining feature of such methods is that for every iteration,

a trial value is proposed for a variable subject to constraints, and violation of these constraints is checked for this value. If the trial value lies outside the feasible set, it is projected back to the boundary of the set, this projection is what is called the return map. This methodology was first applied to the augmented Lagrangian formulation of frictional contact mechanics in [28].

The central idea of the augmented Lagrangian-based return map is to define a trial value of the contact traction at every iteration, where the trial value is defined as the sum of the traction at the previous iteration and a penalty term monitoring the constraints on the normal and tangential displacement jumps. The penalty term, together with the return map, should augment the contact traction until the constraints on the displacement jumps converge, in which case the traction should also converge. In view of this, the trial values should be, at some iteration k :

$$\lambda_n^{\text{trial}} = \lambda_n^{(k)} + c([[\mathbf{u}^{(k+1)}]]_n - g(\mathbf{u}^{(k+1)})), \quad (29a)$$

$$\lambda_\tau^{\text{trial}} = \lambda_\tau^{(k)} + c[[\dot{\mathbf{u}}^{(k+1)}]]_\tau, \quad (29b)$$

for some $c > 0$. These formulas result in the contact traction converging in the case when $[[\mathbf{u}]]_n - g \rightarrow 0$ and $[[\dot{\mathbf{u}}]]_\tau \rightarrow \mathbf{0}$ (stick), while the remaining cases (open, slip) are handled by the return map. Some new notation is introduced at this point: We separate the contact traction λ from the rest of the unknowns, and denote the "residual unknowns" by \mathbf{r} . As we have previously defined the total collection of unknowns as \mathbf{x} , we may write $\mathbf{x} = (\mathbf{r}, \lambda)$. The residual system (22) is accordingly rewritten as $G(\mathbf{r}, \lambda) = \mathbf{0}$. Using this notation, we formulate the return map method below, which is a variant of the method from [28]. We emphasize that the return map is only performed *implicitly* in the method (this point will be expanded upon), hence we call it the *implicit return map method* (IRM).

Algorithm 2 Implicit Return Map Method (IRM)

1. Pick an initial guess $\mathbf{x}^0 = (\mathbf{r}^0, \lambda^0)$. Set $k = 0$.
2. Solve the following system for $(\mathbf{r}^{(k+1)}, \lambda^{(k+1)})$:

$$G(\mathbf{r}^{(k+1)}, \lambda^{(k+1)}) = \mathbf{0}, \quad (30)$$

where $\lambda^{(k+1)}$ is given by the following return map:

$$\lambda_n^{(k+1)} = \begin{cases} \lambda_n^{\text{trial}} & \text{if } \lambda_n^{\text{trial}} \leq 0, \\ 0 & \text{if } \lambda_n^{\text{trial}} > 0, \end{cases} \quad (31a)$$

$$\lambda_\tau^{(k+1)} = \begin{cases} \lambda_\tau^{\text{trial}} & \text{if } \|\lambda_\tau^{\text{trial}}\| \leq b^{(k+1)}, \\ b^{(k+1)} \frac{\lambda_\tau^{\text{trial}}}{\|\lambda_\tau^{\text{trial}}\|} & \text{if } \|\lambda_\tau^{\text{trial}}\| > b^{(k+1)}, \end{cases} \quad (31b)$$

where $b^{(k+1)} = -F\lambda_n^{(k+1)}$.

3. Convergence check:
if $(\mathbf{r}^{(k+1)}, \lambda^{(k+1)})$ fulfills convergence criterion **then**
Exit algorithm.
else
Set $k = k + 1$ and go to 2.
-

Note that algorithm 2 defines a nested loop; each outer iteration k corresponds to an inner loop for solving the (in general nonlinear) system (30) together with the return map (31). We observe that the return map is implicit due to the presence of $\lambda^{(k+1)}$ in (30), meaning that (30) and (31) must be solved simultaneously.

We will now provide a connection between the return maps (31a) and (31b) and the complementarity functions (23) and (24), which leads to a practical way of solving the system (30) and (31). The key observation is that the return maps can be reformulated using max-functions. Additionally, we need to define the characteristic function $\chi^{(k+1)}$, equal to one if $b^{(k+1)} = 0$ and zero if $b^{(k+1)} > 0$. Note that $b^{(k+1)}$ will always be non-negative, since the return map ensures that $\lambda_n^{(k+1)} \leq 0$. Using this notation,

equations (31a) and (31b) can be rewritten as:

$$\lambda_n^{(k+1)} = -\max(0, -\lambda_n^{\text{trial}}), \quad (32a)$$

$$\boldsymbol{\lambda}_\tau^{(k+1)} = \frac{(\chi^{(k+1)} - 1)b^{(k+1)}\boldsymbol{\lambda}_\tau^{\text{trial}}}{(\chi^{(k+1)} - 1)\max(b^{(k+1)}, \|\boldsymbol{\lambda}_\tau^{\text{trial}}\|) + \chi^{(k+1)}}. \quad (32b)$$

The characteristic function is needed to avoid division by zero in the case when $b^{(k+1)} = \|\boldsymbol{\lambda}_\tau^{\text{trial}}\| = 0$. If we now further rewrite (32) to residual form and substitute the definitions of the trial tractions, we obtain:

$$\lambda_n^{(k+1)} + \max(0, -\lambda_n^{(k)} - c([\mathbf{u}^{(k+1)}]_n - g(\mathbf{u}^{(k+1)}))) = 0, \quad (33a)$$

$$\chi^{(k+1)}\boldsymbol{\lambda}_\tau^{(k+1)} + (1 - \chi^{(k+1)}) \left[b^{(k+1)}(\boldsymbol{\lambda}_\tau^{(k)} + c[[\dot{\mathbf{u}}^{(k+1)}]]_\tau) - \max(b^{(k+1)}, \|\boldsymbol{\lambda}_\tau^{(k)} + c[[\dot{\mathbf{u}}^{(k+1)}]]_\tau\|)\boldsymbol{\lambda}_\tau^{(k+1)} \right] = \mathbf{0}. \quad (33b)$$

Equations (33a) and (33b) are nearly identical to the complementarity functions (23) and (24); the only difference is the terms involving the traction at the previous iteration, $\boldsymbol{\lambda}^{(k)}$, which is a known quantity in these equations. One can interpret (33a) and (33b) as regularized contact conditions, in the sense that they convert the contact conditions from graphs to functions, due to the $\boldsymbol{\lambda}^{(k)}$ -terms. Hence, IRM is equivalent to solving a sequence of systems with regularized contact conditions. More precisely, for a fixed $\boldsymbol{\lambda}^{(k)}$ one may define the regularized complementarity functions

$$\begin{aligned} \mathcal{C}_n^{(k)} &:= \lambda_n + \max(0, -\lambda_n^{(k)} - c([\mathbf{u}]_n - g(\mathbf{u}))), \\ \mathcal{C}_\tau^{(k)} &:= \chi\boldsymbol{\lambda}_\tau + (1 - \chi) \left[b(\boldsymbol{\lambda}_\tau^{(k)} + c[[\dot{\mathbf{u}}]]_\tau) - \max(b, \|\boldsymbol{\lambda}_\tau^{(k)} + c[[\dot{\mathbf{u}}]]_\tau\|)\boldsymbol{\lambda}_\tau \right]. \end{aligned}$$

Iteration k of IRM then amounts to solving for $\mathbf{x}^{(k+1)}$ the following regularized version of system (25):

$$\begin{bmatrix} G(\mathbf{x}^{(k+1)}) \\ \mathcal{C}_n^{(k)}(\mathbf{x}^{(k+1)}) \\ \mathcal{C}_\tau^{(k)}(\mathbf{x}^{(k+1)}) \end{bmatrix} = \mathbf{0}. \quad (34)$$

These regularized systems may be solved by GNM (algorithm 1), and this is how IRM has been implemented in practice in the numerical experiments of section 4. We note also that the return map (31) is equivalent to updating the contact tractions (or augmented Lagrange multipliers) by fixed-point iteration, according to (32). This corresponds to the classical *Uzawa* algorithm [22]. Hence, IRM can also be interpreted as an Uzawa algorithm. Again we emphasize that the fixed-point iteration is only performed implicitly in IRM, resulting in an implicit Uzawa algorithm. It is known that for purely mechanical contact problems, implicit Uzawa algorithms converge for a larger range of augmentation parameters than their explicit counterparts [29], at the cost of needing to solve a larger and more complicated system.

The augmentation parameter c takes on a different meaning for IRM, compared to GNM. Here it directly controls the strength of the regularization, and as $c \rightarrow \infty$, the regularized complementarity functions (33a) and (33b) converge to the exact functions (23) and (24). However, like GNM, the augmented Lagrangian formulation ensures that IRM also converges to the non-regularized solution for any $c > 0$, although in this case the convergence speed is highly dependent on the value of c , with lower values requiring more iterations of the outer loop to converge. This is a well-known feature of Uzawa algorithms [24, 29].

Similarly to how the sets (28) describing the different contact states could be defined in relation to the original complementarity functions, we can for each outer iteration k of IRM define the "regularized" contact states,

$$\begin{aligned} \text{Regularized open} &= \{-\lambda_n^{(k)} - c([\mathbf{u}^{(k+1)}]_n - g(\mathbf{u}^{(k+1)})) \leq 0\}, \\ \text{Regularized stick} &= \{b^{(k+1)} > 0 \text{ and } \|\boldsymbol{\lambda}_\tau^{(k)} + c[[\dot{\mathbf{u}}^{(k+1)}]]_\tau\| < b^{(k+1)}\}, \\ \text{Regularized slip} &= \{b^{(k+1)} > 0 \text{ and } \|\boldsymbol{\lambda}_\tau^{(k)} + c[[\dot{\mathbf{u}}^{(k+1)}]]_\tau\| \geq b^{(k+1)}\}, \end{aligned} \quad (35)$$

corresponding to the different arguments of the maximum functions of the regularized complementarity functions (33a) and (33b). References to these sets will be made in the numerical experiments of section 4.

3.3 A generalized Newton method with a return map

In the previous section, we showed a connection between the implicit return map method, the generalized Newton method and the complementarity functions. These observations provide the motivation for a new type of nonlinear solver, which we propose in this section. The idea is to design a quasi-Newton method that incorporates the return map (31) of the contact tractions, but without needing to regularize the contact conditions. This can be achieved if, rather than defining the return map implicitly through regularization of the complementarity functions, as done in IRM, we keep the original complementarity functions, and instead perform the return map (31) explicitly after applying an iteration of algorithm 1 (GNM). In place of (29), the trial traction is now defined as the newly obtained guess of the traction from applying one iteration of GNM. Performing the return map in this way removes the need to solve a sequence of regularized systems, and hence also removes the nested loop of IRM. The resulting nonlinear solver is described below, using the notation introduced in section 3.2. We call it the *generalized Newton method with a return map*, and abbreviate it by GNM-RM.

Algorithm 3 Generalized Newton Method with a Return Map (GNM-RM)

1. Pick an initial guess $\mathbf{x}^0 = (\mathbf{r}^0, \boldsymbol{\lambda}^0)$. Set $k = 0$.
 2. Using the generalized Newton method, perform one iteration on the system (25) to get $(\mathbf{r}^{(k+1)}, \boldsymbol{\lambda}^{\text{trial}})$.
 3. Convergence check:
if $(\mathbf{r}^{(k+1)}, \boldsymbol{\lambda}^{\text{trial}})$ fulfills convergence criterion **then**
Exit algorithm.
else
Return map in normal direction:

$$\lambda_n^{(k+1)} = \begin{cases} \lambda_n^{\text{trial}} & \text{if } \lambda_n^{\text{trial}} \leq 0, \\ 0 & \text{if } \lambda_n^{\text{trial}} > 0. \end{cases}$$
Return map in tangential direction:
Define the new friction bound $b^{(k+1)} = -F\lambda_n^{(k+1)}$.

$$\boldsymbol{\lambda}_\tau^{(k+1)} = \begin{cases} \boldsymbol{\lambda}_\tau^{\text{trial}} & \text{if } \|\boldsymbol{\lambda}_\tau^{\text{trial}}\| \leq b^{(k+1)}, \\ b^{(k+1)} \frac{\boldsymbol{\lambda}_\tau^{\text{trial}}}{\|\boldsymbol{\lambda}_\tau^{\text{trial}}\|} & \text{if } \|\boldsymbol{\lambda}_\tau^{\text{trial}}\| > b^{(k+1)}. \end{cases}$$
Set new guess to $(\mathbf{r}^{(k+1)}, \boldsymbol{\lambda}^{(k+1)})$, set $k = k + 1$ and go to 2.
-

Remark 1 (Derivative of max-function) We have observed empirically that the return map will quite frequently result in cases where $\|\boldsymbol{\lambda}_\tau^{(k+1)} + c[[\dot{\mathbf{u}}^{(k+1)}]]_\tau\| = b^{(k+1)}$, i.e. the two arguments of the maximum-function of (24) are equal. In this case, GNM-RM was found to be more robust if the Jacobian corresponding to the second argument is chosen, and so this is done in all of the simulations in section 4. For GNM and IRM, neither of the two options showed a significant increase or decrease in the robustness of the solvers. Therefore, we arbitrarily choose the Jacobian corresponding to the second argument in case of equal arguments also for GNM and IRM.

It should be noted that there is a fundamental difference in the purpose of the return map for GNM-RM, compared to IRM. For IRM, the return map (31) is used in place of the complementarity functions (23) and (24), while for GNM-RM, the same return map is used *on top of* solving the complementarity functions (23) and (24). Hence, for IRM the return map is an essential part of the solution strategy for finding tractions and displacements that fulfill the contact conditions. However, this is not the case with GNM-RM, as fulfillment of the contact conditions is already handled by performing Newton iterations on the complementarity functions (23) and (24), and so the return map for GNM-RM functions merely as stabilization of GNM.

3.4 Finite volume discretization

We conclude this section with a brief summary of the spatial discretizations used in this work, and the corresponding practical implementation of algorithms 1-3. We follow the discretization schemes described in [8] and the references therein. In short, we employ a family of multi-point finite volume approximations for diffusive terms, while an upwinding scheme is used for advective terms. The grids are simplicial and conforming to the fractures, in the sense that lower-dimensional cells coincide with higher-dimensional faces. In this fully discrete formulation, the residual system (22) becomes a nonlinear system of algebraic equations, while the complementarity functions are enforced cell-wise, resulting in another system of nonlinear algebraic equations. The implementation of the generalized Newton method on the full system (or on the regularized systems in the case of IRM) is now straightforward. In GNM-RM, the return maps are performed cell-wise.

4 Numerical experiments

In this section, we will compare the performance of the three nonlinear solvers presented in section 3, GNM, IRM and GNM-RM, through a series of two- and three-dimensional numerical simulations. Specifically, we simulate pressurized fluid injection in a fractured reservoir, mimicking hydraulic stimulation of a fractured geothermal reservoir in crystalline rock. All of the simulations are run using the mixed-dimensional simulation framework PorePy [30]. Runscripts for reproducing the results of this section can be found in the Docker image in [39]. The precise vertex coordinates of the fractures used in the simulations are reported in the supplementary material of this article.

A central focus of the experiments is to test the sensitivity of the solvers to the value of the augmentation parameter c . There are some recommendations on how to choose this parameter from the literature on purely mechanical contact problems. For IRM, it is well established that higher c -values lead to faster convergence of the outer loop, but usually with more iterations per inner Newton loop [16, 24]. Hence, there is often an optimal intermediate c -value that gives a compromise between the two effects. For GNM, it is recommended in [27, 40] to choose the parameter such that the two terms involving $[[\mathbf{u}]]$ and $\boldsymbol{\lambda}$ in the maximum-functions of (23) and (24) are balanced. However, these recommendations may not be easy to implement in practice. Firstly, it is difficult to assess a priori the optimal intermediate c -value of IRM, as shown in [24]. Secondly, it may be difficult to estimate the ratio of $[[\mathbf{u}]]$ and $\boldsymbol{\lambda}$. For simple fracture network geometries (e.g., isolated fractures), this ratio can be estimated from the boundary conditions and material parameters. However, fracture contact mechanics can alter the stress field such that, for intersecting or close fractures, the actual ratio is far from such estimates. The discrepancies may increase further when adding poromechanical effects. These difficulties motivate the testing of a large range of c -values, and assessing the robustness of the solvers in terms of their sensitivity to the value of c .

For each of the solvers, we report on the total number of nonlinear iterations needed for convergence. By this we mean the total number of linear systems that was solved for the duration of the simulation, keeping in mind that for IRM we additionally need to sum over all outer iterations of the nested loop. For the convergence criteria, we require the Euclidean norms, scaled by cell volumes, of both the nonlinear iteration increments and residuals to be below 10^{-8} . For IRM, the same convergence check is done both in the outer and inner loops (recall that the regularized system of the inner loop is solved by GNM). We set the maximal number of allowed iterations per nonlinear system as 100, and simulations where this threshold is exceeded are declared as non-convergent and labeled by "NC". Another way in which the solvers can fail is if the iterations diverge to infinity. We consider a simulation as diverging to infinity if the norm of the residual exceeds 10^5 and label it by "Div". Finally, we set the maximum number of allowed iterations of the outer loop of IRM to be 150, and simulations exceeding this threshold is labeled by "NCO" (non-convergent outer). If an IRM simulation is labeled "NC" or "Div", it means that GNM in the inner loop failed to converge or diverged to infinity.

An appropriate scaling of the units is used to improve the conditioning of the nonlinear systems. It is found empirically that scaling the unit of mass by 10^9 kg results in the primary variables being close to the same order of magnitude, and generally improves the robustness of all solvers. Hence, this unit scaling is used in all simulations. The material constants used in the simulations are listed in table 2.

Parameter	Symbol	Value	Units
Biot coefficient	α	0.8	-
Friction coefficient	F	0.5	-
Matrix permeability	k	$1.0 \cdot 10^{-15}$	m^2
Reference porosity	ϕ_{ref}	$1.0 \cdot 10^{-2}$	-
Shear modulus	G	$1.7 \cdot 10^{10}$	Pa
Lamé's first parameter	$\lambda_{\text{Lamé}}$	$1.111 \cdot 10^{10}$	Pa
Compressibility	γ	$0.4 \cdot 10^{-9}$	Pa^{-1}
Reference fluid density	ρ_{ref}^f	$1.0 \cdot 10^3$	kgm^{-3}
Solid density	ρ^s	$2.7 \cdot 10^3$	kgm^{-3}
Viscosity	η	$1.0 \cdot 10^{-3}$	Pa s
Residual aperture	a_{ref}	$5.0 \cdot 10^{-4}$	m
Dilation angle	ψ	3, 5 or 7	degrees
Reference pressure	p_{ref}	$2.0 \cdot 10^7$	Pa

Table 2 Material parameters used in the simulations.

4.1 Two-dimensional simulations of fluid injection

In our first series of test cases, we restrict ourselves to two dimensions, and neglect gravitational effects. A domain of size 2000×1000 m is considered, with the fracture network as shown in figure 2. The centermost cell of one of the fractures will be kept at a constant higher pressure, which can be thought of as simulating an injection well (marked by a white dot in the figure). We consider an anisotropic stress regime where pressurization of the injection well will cause fractures to slip and open, creating complex dynamics that challenges the nonlinear solvers.

For the flow boundary conditions, we impose pressure values of 20MPa on all external boundaries. For the mechanical boundary conditions, we fix the bottom boundary (zero displacement), while compressive tractions are imposed on the remaining boundary sides. The traction values correspond to a stress tensor with non-zero values $\sigma_{xx} = -30$ MPa and $\sigma_{yy} = -50$ MPa. These pressures and anisotropic stress values are representative for crystalline rocks around 2 km depth. For all simulations, suitable initial values of the variables are found by first imposing a constant pressure field of 20 MPa everywhere, and solving only the purely mechanical subproblem. The solution to this simpler problem is used as the initial guess for the nonlinear solvers.

We test the effect of imposing four different values of the pressure in the injection well: 20.01, 21, 28 and 30 MPa. For the highest injection pressure, we also test the effect of varying the dilation angle ψ . In all cases, we use a grid containing 33830 total cells (this includes matrix, fracture and interface cells). All simulations are run for a single time step of 0.1 days. We consider only a single time step, as the first time step was typically more difficult than subsequent time steps. Figure 3 shows the performance of the solvers for different values of the augmentation parameter c . Note that the parameter is given in units of GPa/m, in accordance with our scaling of the unit of mass. A detailed plot of the contact states and pressure profile for the 30 MPa case with $\psi = 5^\circ$ is provided in figure 2, showing how the elevated pressure in the injection well causes some of the fractures to slip and open.

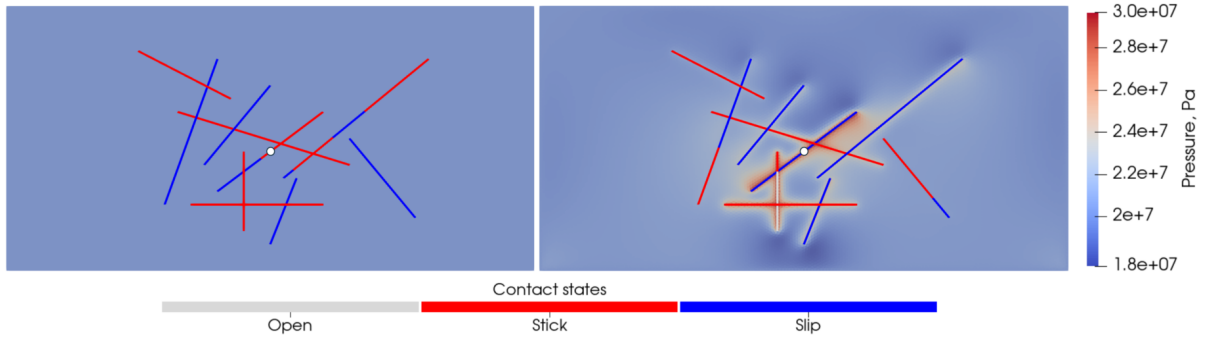


Fig. 2 Visualization of the simulation with an injection pressure of 30 MPa and a dilation angle of 5° , showing the fracture network used in all simulations of section 4.1, and the position of the injection well (the latter is marked by the white dot). Left: Contact states (as defined by (28)) after the initialization stage, but before the injection well is activated. Here, fracture slip is measured relative to a configuration with no deformation. Right: Contact states and pressure profile after activating the injection well and taking a time step of 0.1 days. Here, fracture slip is measured relative to the state after the initialization, i.e. the left figure

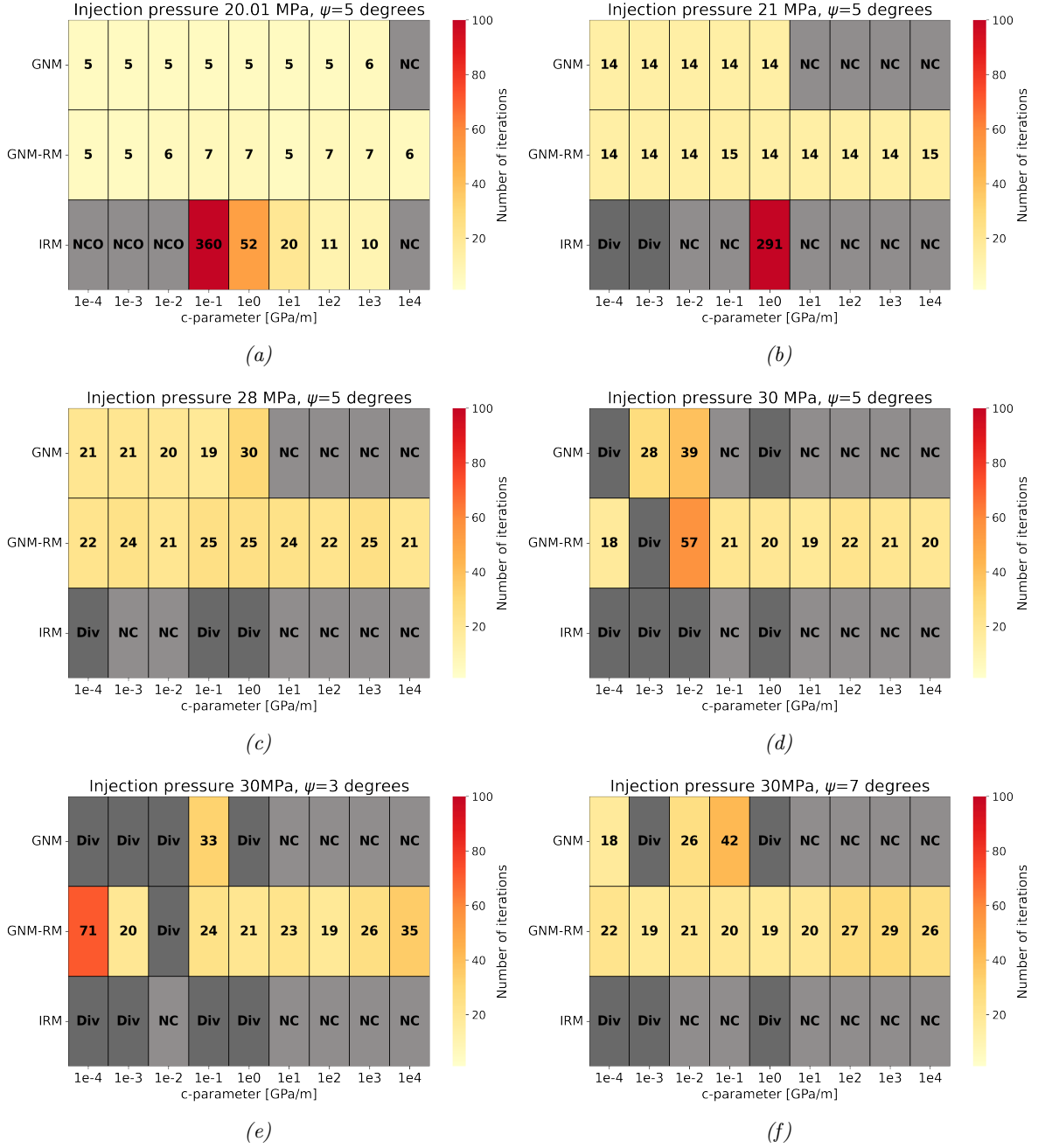


Fig. 3 Number of nonlinear iterations for one time step for the example of section 4.1 with different injection pressures (subfigures 3a-3d) and for different dilation angles (subfigures 3d-3f). NC and Div denote simulations in which the solver did not converge within 100 iterations or diverged to infinity, respectively (for IRM, NC and Div have the same meaning, but applied to GNM in the inner loop). NCO denotes IRM simulations where the outer loop exceeded 150 iterations

From figure 3 it is clear that increasing the injection pressure adds to the difficulty of the problem, with an increase in both the iteration counts, as well as the number of non-convergent cases. For IRM we also have the problem of the outer loop being significantly slower for lower values of c , with some cases terminating due to the outer loop using more than 150 iterations. In the simplest case, figure 3a, corresponding to an injection pressure of 20.01 MPa, we can observe the optimal value of $c = 10^3$ occurring as a compromise between faster outer loops but more difficult inner Newton loops, with the inner Newton loop simply failing to converge for the highest c -value. As previously mentioned, such an optimal c -value is well established in the contact mechanics literature. However, the pattern is immediately broken in the next simplest case, figure 3b (injection pressure 21 MPa), as the inner

Newton loop of IRM fails to converge in all cases, except when $c = 1$. For the more difficult cases, the inner Newton loop does not converge at all. The fact that IRM converges in far fewer cases than GNM suggests that regularizing the complementarity functions actually increases the difficulty of the system. It is clear that IRM is outclassed by the other solvers here. Therefore, we will omit IRM from the rest of the numerical experiments.

GNM appears to handle the smaller values of c better than the larger ones, with c -values of 10 and above only being successful in the simplest case with the 20.01 MPa injection pressure. For the three lowest injection pressures, the method is quite consistent, in terms of the lower c -values consistently resulting in convergence, and the number of iterations being relatively similar across these values. However, the method becomes more unpredictable for the most difficult cases with the 30 MPa injection pressure, both in terms of which c -values that result in convergence, and the number of iterations needed. The method overall seems to have the highest chance of converging for c -values from around 10^{-2} to 10^{-1} GPa/m, as these are the values with the overall fewest number of non-convergent cases. A closer inspection of the solution values reveals that the ratio $\lambda/[[\mathbf{u}]]$, when both are nonzero, is typically in the range from 10^{-2} to 1 GPa/m for the examples of this section. Hence, the recommendation from [27, 40] of choosing c -values that balance the scales of $[[\mathbf{u}]]$ and λ is a relatively good fit to these simulations. However, as mentioned, convergence is far from guaranteed for the most difficult cases, even for c -values in this range.

Moreover, figures 3e and 3f show that GNM can also be sensitive to small changes in the input data, as slight variations in the dilation angle can cause a convergent case to stop converging, or vice versa. It appears that decreasing the dilation angle increases the difficulty of the problem in this case, but the opposite effect has also been reported for other setups [41]. Finally, GNM-RM has the overall best performance out of the three solvers, converging across the largest range of c -values. In particular, it handles the larger c -values much better than the other two solvers. However, like GNM, it also becomes unpredictable for the most difficult setups, in terms of which c -values that result in convergence, and the number of iterations needed. The performance of GNM-RM can also be sensitive to small changes in the input data, such as the dilation angle, as seen in figures 3e and 3f.

A common problem with Newton methods is cycling; in several of the cases in figure 3 where GNM and IRM fail to converge, but without the residual diverging to infinity, the problem is cycling. It appears to be particularly prevalent when a high c -value is used. An example of this is shown in figures 4 and 5, in which data from the simulation with an injection pressure of 28 MPa and a c -value of 10^2 is plotted, corresponding to the results of the seventh column of figure 3b. Figure 4a plots the norm of the total residual vector for the three solvers. The cycling of GNM and IRM is illustrated by repetitive patterns in the residual history. In figure 4b, we show the effect of switching from GNM to GNM-RM, by turning on the return map after 20 iterations. Switching to GNM-RM results in convergence, indicating that GNM-RM can successfully avoid the cycle.

Moreover, the cycling of GNM and IRM occurs nearly always between different contact states, as defined by (28) for GNM and by (35) for IRM. This corresponds to cycling between different arguments of the maximum functions in the complementarity functions. Figure 5 plots the total number of fracture cells residing in each contact state for the three solvers. We observe that for both GNM and IRM, some of the cells cycle between the different states, while GNM-RM avoids the cycle and converges on a fixed number of cells in each contact state.

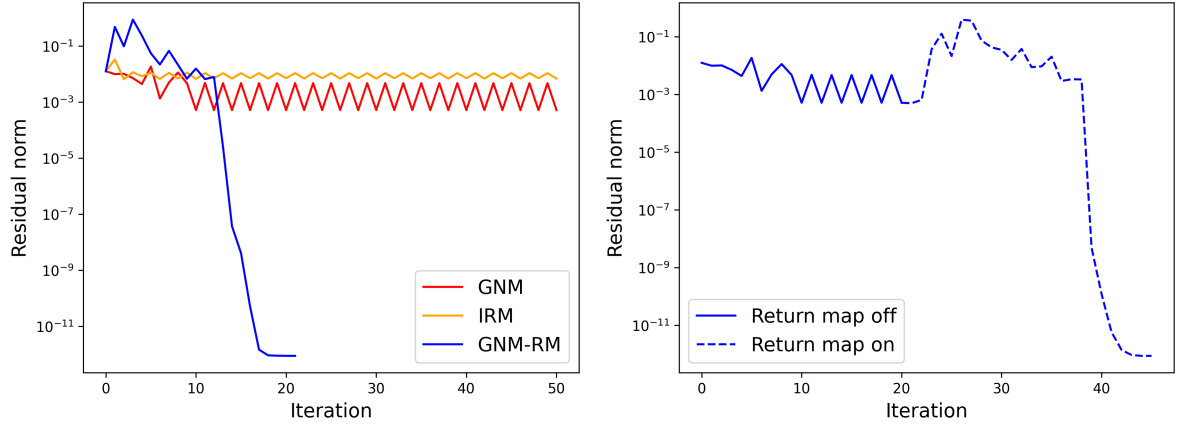


Fig. 4 Residual plots for the different solvers for the simulation with an injection pressure of 28 MPa and c -value of 10^2 , corresponding to column 7 of figure 3c. Left: Residual norms at every iteration for GNM, IRM and GNM-RM. Only the first 50 iterations of GNM and IRM are shown. Right: The same GNM cycle as in the left figure, showing how the cycle can be broken by switching to GNM-RM

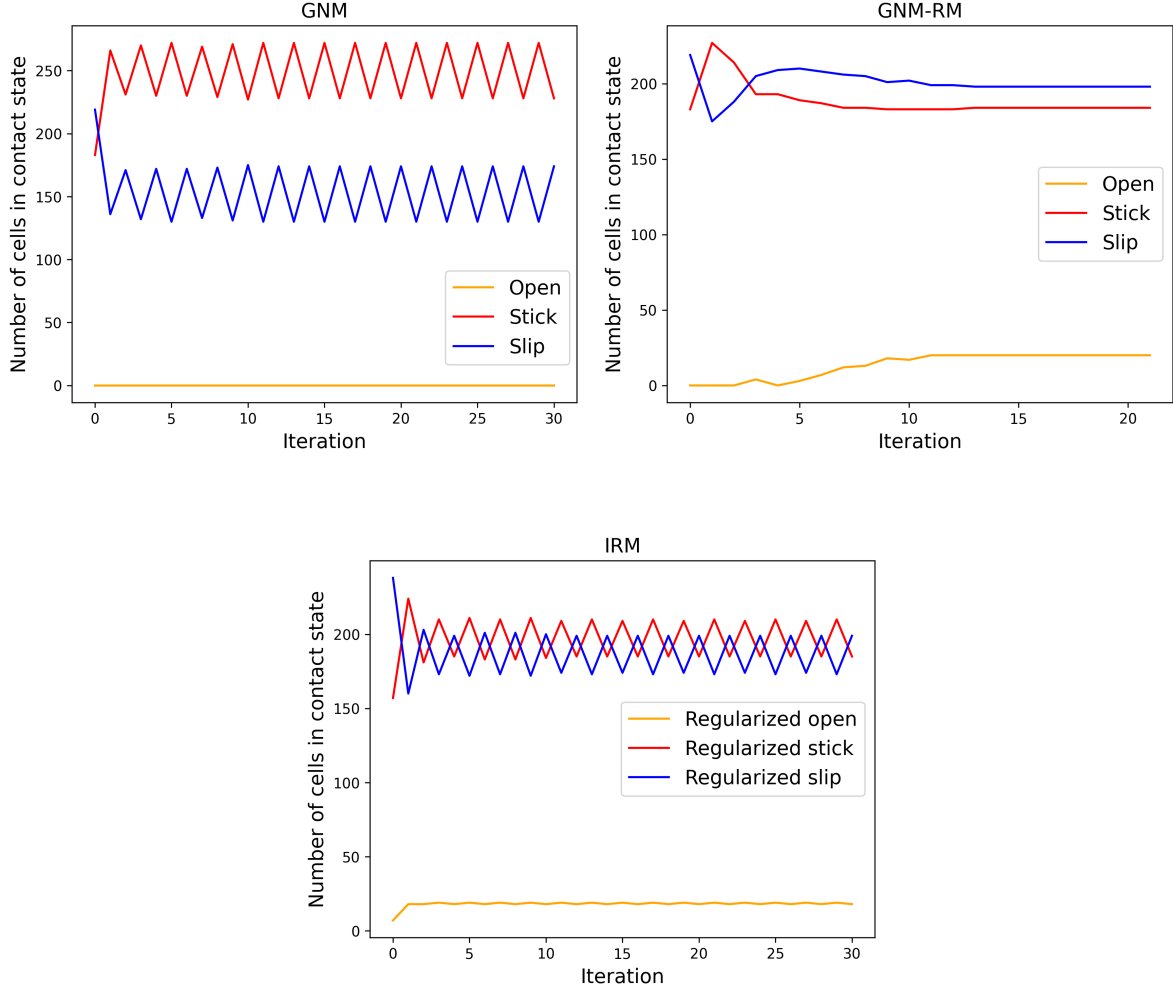


Fig. 5 Number of cells in each contact state for the different solvers for the simulation with an injection pressure of 28 MPa and c -value of 10^2 , corresponding to column 7 of figure 3c. The contact states are defined by the sets (28) for GNM and GNM-RM, while for IRM, the contact states are "regularized" and defined by (35)

Next, we check the scalability of GNM and GNM-RM with respect to the grid size. Using the same fracture network as before, a sequence of four grids is considered: Starting from the grid with 33830 total cells used in the previous simulations, we consider finer grids of 64068, 121501 and 199282 total cells, respectively. The grids are constructed independently of each other. Special attention must be paid to the injection well in order to make the physical setup as similar as possible for the different grids. For each grid we will consider a fracture cell as an injection cell if its center is within the bounds of the injection cell of the coarsest grid, thus ensuring the spatial extent of the elevated pressure corresponding to the injection to be close to constant for all grids.

We run the grid refinement for three cases: One simpler case with an injection pressure of 21 MPa and two more difficult cases with injection pressures of 30 MPa. In the simpler case, we set $c = 10^{-2}$ and $\psi = 5^\circ$, corresponding to the third column of figure 3b. For the other two cases, we use $c = 10^{-2}$, $\psi = 5^\circ$ and $c = 10^{-1}$, $\psi = 3^\circ$, corresponding to the third and fourth columns of figures 3d and 3e, respectively. To make the grid dependency clearer, we now run more than one time step; specifically, we run the simulations for ten time steps, using a constant step size of 0.1 days. The cumulative iteration counts across all time steps are reported in figure 6.

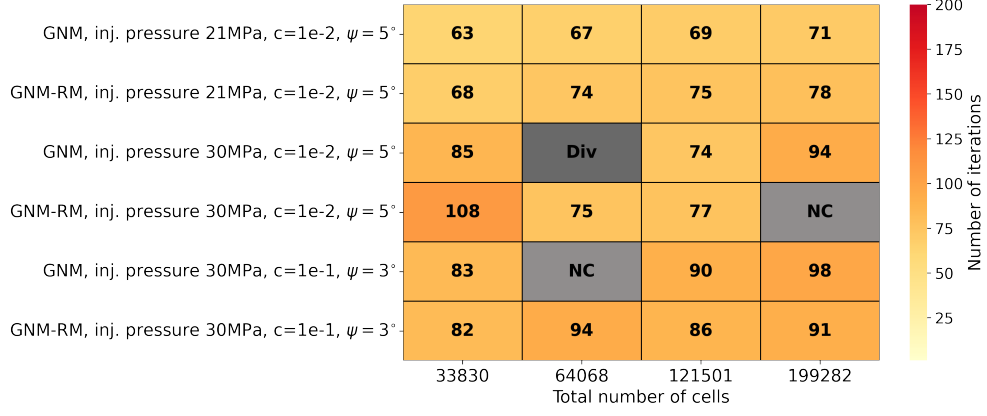


Fig. 6 Cumulative number of iterations over ten time steps, as a function of the grid size.

The results of the simplest case (21 MPa injection pressure) indicate a weak dependency on the grid resolution, showing a modest increase in the total number of iterations for finer grids for both GNM and GNM-RM. A similar weak grid resolution dependency was reported for GNM in [24] for purely mechanical contact problems in non-fractured media. The more difficult cases (30 MPa injection pressure) deviate from this pattern, however, including some non-convergent cases. Note that all of the non-convergent cases fail to converge during the first time step. These observations are similar to the pattern observed in figure 3, namely that as the problem becomes more complex (in this case meaning higher injection pressure), the nonlinear solvers become more unpredictable, and deviate from established results in the contact mechanics literature. Moreover, the results of figure 6 show that changes to the grid structure, caused by the grids being constructed independently, can change the convergence behavior. The influence of the precise grid structure on the convergence behavior for problems of fractured porous media has been noted before in [42].

4.2 Three-dimensional simulations of fluid injection

Next, the solvers will be tested on a three-dimensional problem. As in the previous section, we aim to simulate hydraulic stimulation of critically stressed fractures by an injection well. The domain is the box $(0\text{m}, 2000\text{m}) \times (0\text{m}, 2000\text{m}) \times (-3000\text{m}, -1000\text{m})$, and contains a network of three intersecting, elliptic-shaped fractures, as shown in figure 7. For the hydraulic boundary conditions, we impose hydrostatic pressure conditions on all external boundaries, given by $p = \rho_{\text{ref}}^f g z$, with z being the depth and g the gravitational acceleration. For the mechanical boundary conditions, we fix the bottom boundary (zero displacement), while for the remaining boundaries, we impose compressive tractions, with a similar anisotropy as used in section 4.1. Namely, the corresponding non-zero stress tensor values are:

$$\sigma_{xx} = -0.6\rho^s g z \quad , \quad \sigma_{yy} = -0.6\rho^s g z \quad , \quad \sigma_{zz} = -\rho^s g z. \quad (36)$$

The rest of the simulation setup is similar to that of section 4.1. We will keep the centermost cell of one of the fractures at a constant higher pressure to mimic an injection well (indicated by the vertical black line in figure 7). We test three different injection pressures, by adding 1, 8 and 10 MPa to the background hydrostatic pressure in the injection cell, respectively. The dilation angle is set to 5° for all simulations. Initial values of the variables are found by imposing a constant hydrostatic pressure field and solving only the purely mechanical subproblem. Again we take a single time step, of size 0.1 days.

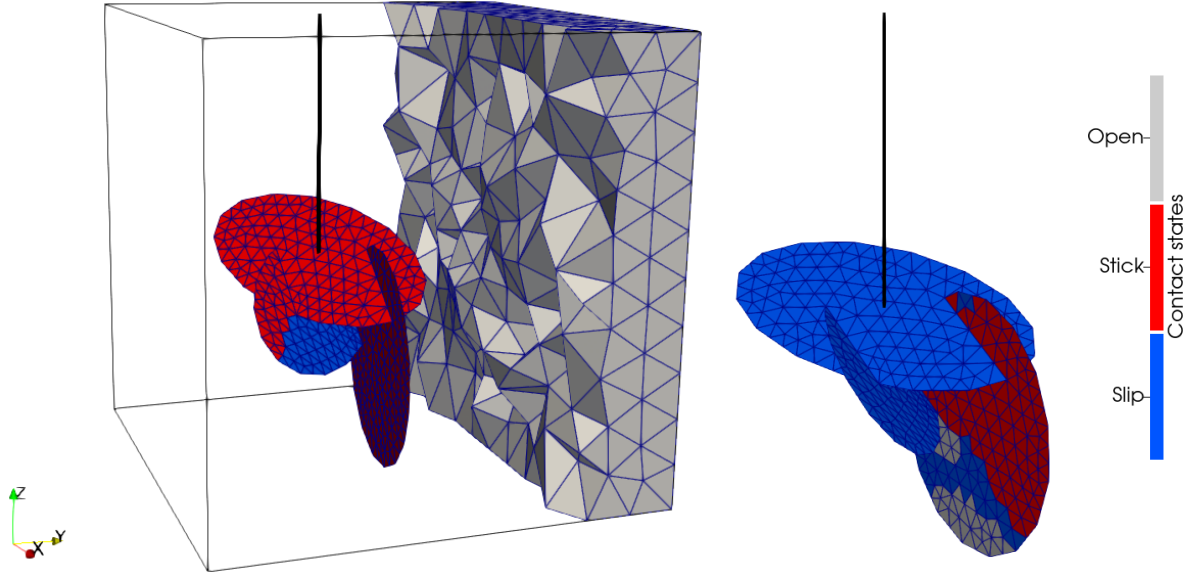


Fig. 7 Left: Fracture network geometry used in the three-dimensional simulations, and the position of the injection well, marked by the vertical black line. Also shown are the two-dimensional grid cells, as well as parts of the three-dimensional grid. Finally, the contact states (as defined by (28)) after the initialization phase are also partially shown, where fracture slip is measured relative to a configuration with no deformation. A total of 702 cells are sticking, and 112 cells are slipping. Right: Contact states after a time step of 0.1 days, for the injection pressure of 30 MPa. A total of 55 cells are open, 179 cells are sticking, and 580 cells are slipping. As before, fracture slip is measured relative to the state after the initialization

The performance of the solvers (but now excluding IRM) for different values of the augmentation parameter and for the three different injection pressures, is shown in figure 8. We observe relatively similar behavior to the two-dimensional case. Increasing the injection pressure causes an increase in the iteration counts, as well as the number of cases not converging. For the two lowest injection pressures, we observe GNM being quite consistent for the lower c -values, but failing to converge for the higher values, while GNM-RM converges across a larger range of c -values, including the higher ones. These are the same results as observed for the lower injection pressures in the two-dimensional example (figures 3a-3c).

However, we once again see the pattern being broken for the most difficult case, with the convergence behavior being more erratic. In particular, GNM-RM fails to converge in all cases. Investigation of the residual norms for a particular case (we checked for $c = 10^3$) reveals that Newton once again enters a cycle. This cycle is avoided by GNM, but its residual norm nonetheless fails to fall below the threshold within 100 iterations. We conclude from these observations that, while GNM-RM displays in many cases added robustness with respect to the augmentation parameter, this is not necessarily always the case.

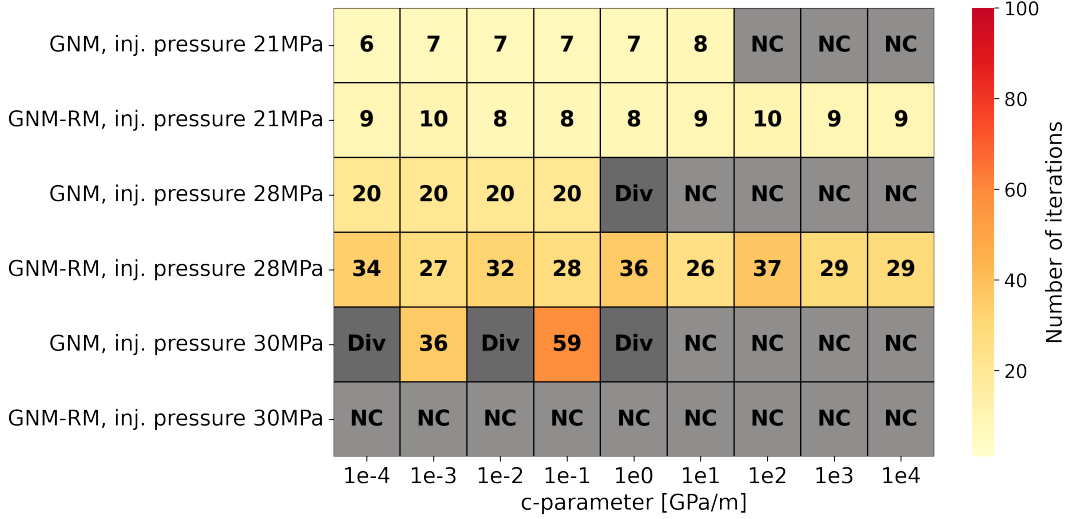


Fig. 8 Iteration counts for one time step for the example of section 4.2 with different injection pressures. NC and Div denote simulations where the solver did not converge within 100 iterations or diverged to infinity, respectively

5 Conclusion

We have investigated the performance of three different nonlinear solvers, all based on the augmented Lagrangian formulation of frictional contact mechanics, for solving advanced problems of coupled flow and deformation in fractured porous media, including fracture contact mechanics. This included two classical solvers, namely the generalized Newton method (GNM) using complementarity functions, and the implicit return map method (IRM). In addition, we have proposed a new nonlinear solver, which essentially combined the two classical solvers. Specifically, the new nonlinear solver incorporated the return map into the generalized Newton method as a postprocessing step after every iteration. It was subsequently named the "generalized Newton method with a return map" (GNM-RM). The purpose of the return map in GNM-RM was to stabilize the generalized Newton method, which is in contrast to classical return map methods like IRM, where its purpose is to ensure the feasibility of the contact tractions.

The performance of the three solvers was assessed through a series of numerical experiments, both two- and three-dimensional, which were designed to mimic hydraulic stimulation of a fractured geothermal reservoir. Key questions included the assessment of the robustness and sensitivity of the performance with respect to the augmentation parameter, as well as grid resolution. The experiments indicated that convergence issues are easily encountered, even for relatively simple fracture geometries. For the simplest numerical experiments, the two classical solvers, GNM and IRM, behaved more or less as expected and in accordance with established heuristics from the contact mechanics literature, regarding the augmentation parameter. However, as the experiments became more complex and strongly coupled, the two solvers behaved more erratically, being very sensitive to the value of the augmentation parameter, and to small changes in the input data (as shown by varying the shear dilation angle). In particular, IRM failed to converge in nearly all cases, except for the very simplest experiment. The new solver, GNM-RM, performed in most cases more robustly with respect to the augmentation parameter, and in particular, it handled larger values of the parameter much better than the classical solvers. It was also demonstrated that in some cases where GNM fails to converge due to cycling, the cycle can be avoided by instead using GNM-RM. That being said, convergence issues were also encountered with GNM-RM, particularly in the three-dimensional case, with its behavior again being unpredictable for the most difficult experiments.

In conclusion, for complex problems of mixed-dimensional poromechanics with fracture contact mechanics, we would strongly recommend GNM over IRM. Moreover, GNM-RM can be worthwhile to try if GNM fails to converge, as we have demonstrated that it may converge in cases where GNM fails, and it is easily implemented as a simple modification of GNM. Perhaps more importantly, however, we conclude

that convergence issues with nonlinear solvers pose a significant bottleneck for running realistic simulations of fractured geothermal reservoirs, as established solvers will frequently display unpredictable behavior. Clearly, more work is needed on this topic.

References

- [1] Berre, I., Doster, F., Keilegavlen, E.: Flow in fractured porous media: A review of conceptual models and discretization approaches. *Transport in Porous Media* **130**, 215–236 (2018) <https://doi.org/10.1007/s11242-018-1171-6>
- [2] Viswanathan, H.S., Ajo-Franklin, J., Birkholzer, J.T., Carey, J.W., Guglielmi, Y., Hyman, J., Karra, S., Pyrak-Nolte, L.J., Rajaram, H., Srinivasan, G., *et al.*: From fluid flow to coupled processes in fractured rock: Recent advances and new frontiers. *Reviews of Geophysics* **60**(1), 2021–000744 (2022) <https://doi.org/10.1029/2021RG000744>
- [3] Vaezi, I., Yoshioka, K., De Simone, S., Gómez-Castro, B.M., Paluszny, A., Jalali, M., Berre, I., Rutqvist, J., Min, K.-B., Lei, Q., *et al.*: A review of thermo-hydro-mechanical modeling of coupled processes in fractured rock: From continuum to discontinuum perspective. *Journal of Rock Mechanics and Geotechnical Engineering* (2025) <https://doi.org/10.1016/j.jrmge.2025.04.033>
- [4] Coussy, O.: *Poromechanics*. John Wiley & Sons, Ltd, Chichester (2003). <https://doi.org/10.1002/0470092718>
- [5] Kikuchi, N., Oden, J.T.: *Contact Problems in Elasticity: A Study of Variational Inequalities and Finite Element Methods*. SIAM Studies in Applied and Numerical Mathematics, Philadelphia (1988). <https://doi.org/10.1137/1.9781611970845>
- [6] Berge, R., Berre, I., Keilegavlen, E., Nordbotten, J., Wohlmuth, B.: Finite volume discretization for poroelastic media with fractures modeled by contact mechanics. *International Journal for Numerical Methods in Engineering* **121** (2019) <https://doi.org/10.1002/nme.6238>
- [7] Stefansson, I., Berre, I., Keilegavlen, E.: A fully coupled numerical model of thermo-hydro-mechanical processes and fracture contact mechanics in porous media. *Computer Methods in Applied Mechanics and Engineering* **386**, 114122 (2021) <https://doi.org/10.1016/j.cma.2021.114122>
- [8] Stefansson, I., Varela, J., Keilegavlen, E., Berre, I.: Flexible and rigorous numerical modelling of multiphysics processes in fractured porous media using PorePy. *Results in Applied Mathematics* **21**, 100428 (2024) <https://doi.org/10.1016/j.rinam.2023.100428>
- [9] Novikov, A., Voskov, D., Khait, M., Hajibeygi, H., Jansen, J.D.: A scalable collocated finite volume scheme for simulation of induced fault slip. *Journal of Computational Physics* **469**, 111598 (2022) <https://doi.org/10.1016/j.jcp.2022.111598>
- [10] Garipov, T.T., Karimi-fard, M., Tchelepi, H.A.: Discrete fracture model for coupled flow and geomechanics. *Computational Geosciences* **20**(1), 149–160 (2016) <https://doi.org/10.1007/s10596-015-9554-z>
- [11] Garipov, T.T., Hui, M.H.: Discrete fracture modeling approach for simulating coupled thermo-hydro-mechanical effects in fractured reservoirs. *International Journal of Rock Mechanics and Mining Sciences* **122**, 104075 (2019) <https://doi.org/10.1016/j.ijrmms.2019.104075>
- [12] Beaude, L., Chouly, F., Laaziri, M., Masson, R.: Mixed and Nitsche’s discretizations of Coulomb frictional contact-mechanics for mixed dimensional poromechanical models. *Computer Methods in Applied Mechanics and Engineering* **413**, 116124 (2023) <https://doi.org/10.1016/j.cma.2023.116124>
- [13] Droniou, J., Laaziri, M., Masson, R.: Discretisations of mixed-dimensional thermo-hydro-mechanical models preserving energy estimates. *Journal of Computational Physics* **515**, 113295 (2024) <https://doi.org/10.1016/j.jcp.2024.113295>

- [14] Salimzadeh, S., Paluszny, A., Nick, H.M., Zimmerman, R.W.: A three-dimensional coupled thermo-hydro-mechanical model for deformable fractured geothermal systems. *Geothermics* **71**, 212–224 (2018) <https://doi.org/10.1016/j.geothermics.2017.09.012>
- [15] Franceschini, A., Castelletto, N., White, J.A., Tchelepi, H.A.: Algebraically stabilized Lagrange multiplier method for frictional contact mechanics with hydraulically active fractures. *Computer Methods in Applied Mechanics and Engineering* **368**, 113161 (2020) <https://doi.org/10.1016/j.cma.2020.113161>
- [16] Frigo, M., Tchelepi, H., Castelletto, N., Cusini, M., Settgast, R.: Augmented Lagrangian Method with Bubble Stabilization for Frictional Contact in Poroelastic Media. *SPE Reservoir Simulation Conference*, vol. SPE Reservoir Simulation Conference, pp. 011–004003 (2025). <https://doi.org/10.2118/223896-MS>
- [17] Franceschini, A., Castelletto, N., Ferronato, M.: Block preconditioning for fault/fracture mechanics saddle-point problems. *Computer Methods in Applied Mechanics and Engineering* **344**, 376–401 (2019) <https://doi.org/10.1016/j.cma.2018.09.039>
- [18] Franceschini, A., Gazzola, L., Ferronato, M.: A scalable preconditioning framework for stabilized contact mechanics with hydraulically active fractures. *Journal of Computational Physics* **463**, 111276 (2022) <https://doi.org/10.1016/j.jcp.2022.111276>
- [19] Franceschini, A., Castelletto, N., White, J.A., Tchelepi, H.A.: Scalable preconditioning for the stabilized contact mechanics problem. *Journal of Computational Physics* **459**, 111150 (2022) <https://doi.org/10.1016/j.jcp.2022.111150>
- [20] Zabegaev, Y., Berre, I., Keilegavlen, E., Kumar, K.: An efficient preconditioner for mixed-dimensional contact poromechanics based on the fixed stress splitting scheme. *arXiv preprint* (2025) <https://doi.org/10.48550/arXiv.2501.07441>
- [21] Zabegaev, Y., Berre, I., Keilegavlen, E.: A block preconditioner for thermo-poromechanics with frictional deformation of fractures. *arXiv preprint* (2025) <https://doi.org/10.48550/arXiv.2505.04247>
- [22] Wriggers, P.: *Computational Contact Mechanics*, 2. Aufl. edn. Springer, Berlin, Heidelberg (2006). <https://doi.org/10.1007/978-3-540-32609-0>
- [23] Nejati, M., Paluszny, A., Zimmerman, R.W.: A finite element framework for modeling internal frictional contact in three-dimensional fractured media using unstructured tetrahedral meshes. *Computer Methods in Applied Mechanics and Engineering* **306**, 123–150 (2016) <https://doi.org/10.1016/j.cma.2016.03.028>
- [24] Renard, Y.: Generalized Newton’s methods for the approximation and resolution of frictional contact problems in elasticity. *Computer Methods in Applied Mechanics and Engineering* **256**, 38–55 (2013) <https://doi.org/10.1016/j.cma.2012.12.008>
- [25] Alart, P., Curnier, A.: A mixed formulation for frictional contact problems prone to Newton like solution methods. *Computer Methods in Applied Mechanics and Engineering* **92**(3), 353–375 (1991) [https://doi.org/10.1016/0045-7825\(91\)90022-X](https://doi.org/10.1016/0045-7825(91)90022-X)
- [26] Christensen, P.W., Klarbring, A., Pang, J.S., Strömberg, N.: Formulation and comparison of algorithms for frictional contact problems. *International Journal for Numerical Methods in Engineering* **42**, 145–173 (1998) [https://doi.org/10.1002/\(SICI\)1097-0207\(19980515\)42:1<145::AID-NME358>3.0.CO;2-L](https://doi.org/10.1002/(SICI)1097-0207(19980515)42:1<145::AID-NME358>3.0.CO;2-L)
- [27] Hüeber, S., Stadler, G., Wohlmuth, B.I.: A primal-dual active set algorithm for three-dimensional contact problems with Coulomb friction. *SIAM Journal on Scientific Computing* **30**(2), 572–596 (2008) <https://doi.org/10.1137/060671061>
- [28] Simo, J.C., Laursen, T.A.: An augmented lagrangian treatment of contact problems involving friction. *Computers & Structures* **42**(1), 97–116 (1992) [https://doi.org/10.1016/0045-7949\(92](https://doi.org/10.1016/0045-7949(92)

- [29] Kunisch, K., Stadler, G.: Generalized Newton methods for the 2d-Signorini contact problem with friction in function space. *ESAIM: Mathematical Modelling and Numerical Analysis* **39**(4), 827–854 (2005) <https://doi.org/10.1051/m2an:2005036>
- [30] Keilegavlen, E., Berge, R., Fumagalli, A., Starnoni, M., Stefansson, I., Varela, J., Berre, I.: PorePy: An open-source software for simulation of multiphysics processes in fractured porous media. *Computational Geosciences* **25**, 243–265 (2021) <https://doi.org/10.1007/s10596-020-10002-5>
- [31] Zimmerman, R., Bodvarsson, G.: Hydraulic conductivity of rock fractures. *Transport in Porous Media* **23**, 1–30 (1996) <https://doi.org/10.1007/BF00145263>
- [32] Martin, V., Jaffré, J., Roberts, J.E.: Modeling fractures and barriers as interfaces for flow in porous media. *SIAM Journal on Scientific Computing* **26**(5), 1667–1691 (2005) <https://doi.org/10.1137/S1064827503429363>
- [33] Both, J.W., Brattekås, B., Fernø, M., Keilegavlen, E., Nordbotten, J.M.: High-fidelity experimental model verification for flow in fractured porous media. *InterPore Journal* **1**(3), 271124–6 (2024) <https://doi.org/10.69631/ipj.v1i3nr31>
- [34] Clarke, F.H.: Optimization and Nonsmooth Analysis. Society for Industrial and Applied Mathematics, Philadelphia (1990). <https://doi.org/10.1137/1.9781611971309>
- [35] Souza Neto, E.A., Peric, D., Owen, D.R.J.: Computational Methods for Plasticity. John Wiley and Sons, Ltd, New York (2008). <https://doi.org/10.1002/9780470694626.ch7>
- [36] Simo, J.C., Hughes, T.J.R.: Computational Inelasticity. Springer, New York (1998). <https://doi.org/10.1007/b98904>
- [37] Giannakopoulos, A.E.: The return mapping method for the integration of friction constitutive relations. *Computers & Structures* **32**(1), 157–167 (1989) [https://doi.org/10.1016/0045-7949\(89\)90081-3](https://doi.org/10.1016/0045-7949(89)90081-3)
- [38] Wriggers, P., Vu Van, T., Stein, E.: Finite element formulation of large deformation impact-contact problems with friction. *Computers & Structures* **37**(3), 319–331 (1990) [https://doi.org/10.1016/0045-7949\(90\)90324-U](https://doi.org/10.1016/0045-7949(90)90324-U)
- [39] Nevland, M., Berre, I., Keilegavlen, E., Both, J.W.: Source code: Augmented Lagrangian Solvers for Poroelasticity with Fracture Contact Mechanics. <https://doi.org/10.5281/zenodo.16881390>
- [40] Gitterle, M., Popp, A., Gee, M., Wall, W.: Finite deformation frictional mortar contact using a semi-smooth Newton method with consistent linearization. *International Journal for Numerical Methods in Engineering* **84**, 543–571 (2010) <https://doi.org/10.1002/nme.2907>
- [41] Stefansson, I.: A line search algorithm for multiphysics problems with fracture deformation. *InterPore Journal* **1**(3), 271124–7 (2024) <https://doi.org/10.69631/ipj.v1i3nr33>
- [42] Ucar, E., Keilegavlen, E., Berre, I., Nordbotten, J.M.: A finite-volume discretization for deformation of fractured media. *Computational Geosciences* **22**, 993–1007 (2018) <https://doi.org/10.1007/s10596-018-9734-8>